






## Enhanced mobility of ternary InGaAs quantum wells through digital alloying

Jason T. Dong <sup>1</sup>, Yilmaz Gul <sup>2</sup>, Aaron N. Engel,<sup>1</sup> Teun A. J. van Schijndel,<sup>3</sup> Connor P. Dempsey <sup>3</sup>,  
Michael Pepper <sup>2,4</sup> and Christopher J. Palmström <sup>1,3,\*</sup>

<sup>1</sup>Materials Department, University of California, Santa Barbara, California 93106, USA

<sup>2</sup>London Centre for Nanotechnology, University College London, 17-19 Gordon Street, London WC1H 0AH, United Kingdom

<sup>3</sup>Department of Electrical and Computer Engineering, University of California, Santa Barbara, California 93106, USA

<sup>4</sup>Department of Electronic and Electrical Engineering, University College London, Torrington Place, London WC1E 7JE, United Kingdom



(Received 1 April 2024; accepted 5 June 2024; published 26 June 2024)

High In content InGaAs quantum wells ( $\text{In} \geq 75\%$ ) are potentially useful for topological quantum computing and spintronics applications. In high-mobility InGaAs quantum wells, alloy disorder scattering is a limiting factor. In this paper, we demonstrate that by growing the InGaAs quantum wells as a digital alloy, or a short period superlattice, we can reduce the alloy disorder scattering within the quantum well and increase the peak 2 K electron mobility to  $545\,000\text{ cm}^2/\text{Vs}$ , which is the highest reported mobility for high-In content InGaAs quantum wells to the best of the authors' knowledge. Our results demonstrate that the digital alloy approach can be used to increase the mobility of quantum wells in random alloy ternary materials.

DOI: [10.1103/PhysRevMaterials.8.064601](https://doi.org/10.1103/PhysRevMaterials.8.064601)

### I. INTRODUCTION

InGaAs quantum wells with high In content ( $\text{In} \geq 75\%$ ) have a smaller electron effective mass, smaller band gap energy, larger  $g$  factor [1], and larger spin-orbit coupling [2,3] compared to GaAs quantum wells. These properties of InGaAs quantum wells make high electron mobility quantum wells promising materials for topological quantum computing [4,5] and spintronics [6]. While alloying the GaAs with InAs both enables the tunability of the properties and enhances certain properties of the quantum wells, it introduces random alloy disorder in the material. This intrinsic random alloy disorder leads to alloy disorder scattering of charge carriers and is a limiting factor in high electron mobility InGaAs quantum wells. The current state-of-the-art mobilities in high-In content InGaAs quantum wells is  $\sim 430\,000\text{ cm}^2/\text{Vs}$  [7] and alloy disorder scattering is a major scattering mechanism near the peak mobility [7,8]. Reducing this intrinsic alloy disorder scattering poses a significant challenge towards improving the mobilities of InGaAs quantum wells.

Digital alloys (DA) are an alternative approach to alloying by growing the material as a short period superlattice [9] instead of a random alloy. While the properties of digital alloys often closely resemble that of the random alloys, properties such as the band gap [9–11] and effective mass [12] can vary significantly. Digital alloys have been predominantly implemented in optoelectronic devices such as low excess noise avalanche photodetectors [13] and low series resistance distributed Bragg reflectors [14]. There have been some studies on the transport of heterostructures grown with digital alloys, such as magnetically doped semiconductor quantum wells [15], parabolic quantum wells [16], and coupled multiple quantum wells [17,18]. Digital alloys are potentially

promising in improving the transport mobility of semiconductor alloys. By growing a digital alloy as an ordered structure comprised of binary semiconductors, which intrinsically do not possess any alloy disorder, it is expected that there is no alloy disorder scattering within the material and the transport mobility will increase [19,20]. However, a systematic investigation in the effects of digital alloying on the alloy disorder scattering of charge carrier transport has yet to be performed.

In this study, we compare random and digital alloy InGaAs quantum wells grown metamorphically on InP substrates. InAs/GaAs and InAs/InGaAs superlattices are implemented as digital alloy quantum wells. Single sub-band transport with vanishing magnetoresistance is observed in all of the samples, which is indicative of high-quality samples. We find that the InAs/InGaAs DA quantum wells have an enhanced mobility of  $545\,000\text{ cm}^2/\text{Vs}$ , which is the highest reported mobility for high-In content InGaAs quantum well to the best of the authors' knowledge. The mobility of the InAs/GaAs DA quantum well is found to be reduced in comparison to the random alloy sample. By analyzing the scattering mechanisms of the different quantum wells, we attribute the enhancement of the InAs/InGaAs DA mobility due to a reduction in the alloy disorder scattering and the reduction of the InAs/GaAs DA mobility due to increased interfacial roughness and background impurity incorporation. Our results demonstrate that digital alloying is a promising way to improve the mobility of III-V semiconductor alloys, however, care must be made with the growth and design of the digital alloys in order to enhance the mobility.

### II. MBE GROWTH, DEVICE FABRICATION, AND MEASUREMENTS

Samples were grown on epi-ready semi-insulating Fe-doped InP (001) wafers (AXT Inc.) in a VG V80H MBE system. The oxide was desorbed by heating the InP wafers

\*Contact author: [cjpalms@ucsb.edu](mailto:cjpalms@ucsb.edu)

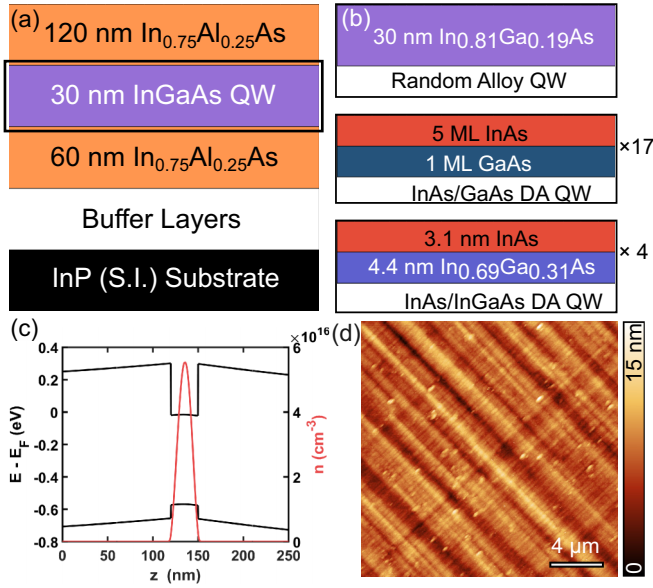


FIG. 1. (a) Sample structure schematic, consisting of a 30 nm thick InGaAs quantum well buried 120 nm from the surface. The quantum wells were grown metamorphically on InP substrates. (b) Different samples in the study: a random alloy quantum well, a 17-period InAs/GaAs digital alloy quantum well, and a four-period InAs/InGaAs digital alloy quantum well. (c) Self-consistent Schrödinger-Poisson simulation of the sample structure. (d) Representative AFM micrograph of InAlAs top barrier, crosshatching typical of metamorphic growth is observed.

under an  $\text{As}^2$  flux until the metal-rich transition to a  $(4 \times 2)$  surface reconstruction was observed by reflection high-energy electron diffraction. This transition is used to calibrate the pyrometer temperature to  $515^\circ\text{C}$ . After oxide desorption, 100 nm of a nearly lattice matched superlattice of 4 nm  $\text{In}_{0.52}\text{Al}_{0.48}\text{As}/1\text{ nm } \text{In}_{0.52}\text{Ga}_{0.48}\text{As}$  was grown at  $480^\circ\text{C}$ . The substrate was then cooled down to  $340^\circ\text{C}$ , and a step graded buffer layer was grown from  $\text{In}_{0.575}\text{Al}_{0.425}\text{As}$  to  $\text{In}_{0.825}\text{Al}_{0.175}\text{As}$  in 50 nm thick steps, where the composition of In would change 2.5% each step. The buffer layer is then reverse stepped to  $\text{In}_{0.75}\text{Al}_{0.25}\text{As}$  in 50 nm thick steps of 2.5% In composition changes.

After the completion of the graded buffer layer, the substrate is heated to a pyrometer temperature of  $470^\circ\text{C}$  where a 60 nm  $\text{In}_{0.75}\text{Al}_{0.25}\text{As}$  bottom barrier, a 30 nm  $\text{In}_{0.81}\text{Ga}_{0.19}\text{As}$  quantum well, and a 120 nm  $\text{In}_{0.75}\text{Al}_{0.25}\text{As}$  top barrier are grown. The layer schematic is shown in Fig. 1(a). The InGaAs quantum well is grown as either a random alloy or a digital alloy, shown schematically in Fig. 1(b). Two different digital alloy quantum wells with a total thickness of 30 nm are grown: an InAs/GaAs digital alloy quantum well consisting of 17 periods of five monolayers of InAs and one monolayer of GaAs and an InAs/InGaAs digital alloy quantum well consisting of four periods of 3.1 nm of InAs and 4.4 nm of  $\text{In}_{0.69}\text{Ga}_{0.31}\text{As}$ . For the digital alloy samples, a 1 s growth interrupt between the layers was included to improve the ordering at the interfaces. The GaAs layer thickness in the InAs/GaAs digital alloy could not exceed one monolayer, growth thicker than one monolayer resulted in the relaxation of the GaAs layer.

The quantum wells are in electron accumulation despite the entire heterostructure being unintentionally doped. This result is consistent with one-dimensional (1D) Schrödinger-Poisson calculations of the band structure, shown in Fig. 1(c), performed using the methods described in Ref. [21] and prior reports on the growth of undoped high-In content InGaAs quantum wells [22,23].

The surface morphology of the InAlAs top barrier is shown in the atomic force micrograph shown in Fig. 1(d). A crosshatched morphology typical of metamorphic growth is observed, with the rms roughness of the InAlAs top barrier over a  $400\ \mu\text{m}^2$  area typically 1–2 nm.

Mesas for Hall bars were fabricated using wet chemical etching with a mixture of  $\text{H}_2\text{SO}_4:\text{H}_2\text{O}_2:\text{H}_2\text{O}$  (1:8:120). Following mesa definition, NiGeAu contacts were deposited and subsequently annealed at  $450^\circ\text{C}$  for 2 min to form ohmic contacts to the quantum well. A 30 nm  $\text{AlO}_x$  gate dielectric was deposited with atomic layer deposition. Finally, a Ti/Au top gate was deposited on the Hall bar. The ratio of the Hall bar width to the spacing of the arms was 9.25. Magnetotransport measurements were performed in a Quantum Design Physical Property Measurement System at 2 K using standard low-frequency ac lock-in measurements, with an ac current of  $0.5\ \mu\text{A}$ . The two-dimensional electron gas (2DEG) carrier density was modulated by applying a voltage to the top gate electrode.

### III. RESULTS AND DISCUSSION

#### A. Quantum well band structure

The band structure of the random and digital alloy quantum wells was computed using the  $k \cdot p$  method for heterostructures with the envelope function approximation, using the methods described in Ref. [24]. The first four conduction band sub-band energies and their associated probability densities ( $|\psi|^2$ ) for the three different samples are plotted in Fig. 2. The  $|\psi|^2$  of the random alloy and the InAs/GaAs DA quantum wells are sinusoidal-like envelope functions over the channel of the quantum well. However, for the  $|\psi|^2$  in the InAs/InGaAs digital alloy, the  $|\psi|^2$  are the sinusoidal-like envelope functions of the quantum well with peaks in the InAs layers and troughs in the InGaAs regions. Although the InAs/InGaAs digital alloy still has alloy disorder present through the use of the InGaAs layers, the overall alloy disorder scattering may be reduced by having the electron preferring to reside in the InAs regions of the digital alloy. The band parameters of the quantum wells are summarized in Table I, which contains the predicted energy gap of the quantum wells, the sub-band spacing between the first and second electron sub-bands, the first sub-band effective mass ( $m^*$ ), and the nonparabolicity factor ( $\alpha$ ).  $\alpha$  is defined with:  $E(1 + \alpha E) = \frac{\hbar^2 k^2}{2m^*}$ , where  $E$  is the Fermi energy and  $k$  is the Fermi wave vector.

From the  $k \cdot p$  calculations, it is expected that sub-bands form in the digital alloy and random alloy quantum wells, with the digital alloy quantum wells having a slightly smaller sub-band spacing than the random alloy quantum wells. The predicted effective masses and nonparabolicity of the quantum wells is not expected to change significantly. However, it is

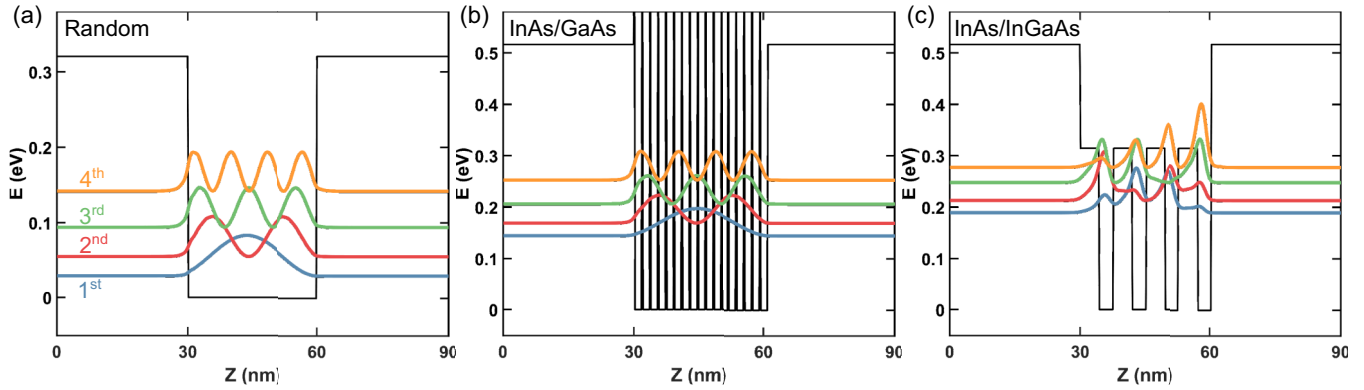


FIG. 2. Plots of the conduction band edges and the  $|\psi|^2$  of the first four conduction band subbands of the: (a) random alloy, (b) InAs/GaAs DA, and (c) InAs/InGaAs DA quantum wells calculated with the  $k \cdot p$  method.

predicted that the InAs/GaAs DA quantum well to have a slightly smaller effective mass compared to the InAs/InGaAs DA and the random alloy quantum wells. The predicted results for the InAs/GaAs DA may be incorrect, as the  $k \cdot p$  method can be less accurate in simulation of monolayer thick heterostructures, which is discussed in depth in Ref. [25].

### B. Magnetotransport

An optical image of a Hall bar used in this study with the schematic wiring diagram is shown in Fig. 3(a). The  $R_{xx}$  and  $R_{xy}$  from  $B = 0$  T to  $B = 14$  T for the random and digital alloy quantum wells is shown in Figs. 3(b)–3(d), with  $n_{2\text{DEG}} = 3.52 \times 10^{11}$ ,  $2.78 \times 10^{11}$ , and  $3.60 \times 10^{11} \text{ cm}^{-2}$  for the random alloy, InAs/GaAs DA, and InAs/InGaAs DA, respectively.  $n_{2\text{DEG}}$  is the sheet electron density extracted from the Hall measurements. The integer quantum Hall effect is observed along with vanishing magnetoresistance for all samples. In both of the digital alloy quantum wells, single band transport is observed and the transport does not resemble the coupled multiple quantum well transport observed in GaAs/AlAs digital alloy quantum wells [17,18]. The Hall resistance of the InAs/GaAs and the InAs/InGaAs samples is quantized to units of  $h/e^2\nu$ , where  $\nu$  is the filling factor. In multiple quantum wells, the Hall resistance is quantized into units of  $h/e^2\nu j$ , where  $j$  is the number of quantum wells [26]. In both the InAs/GaAs and the InAs/InGaAs samples, the observation of the integer quantum Hall effect without the additional  $j$  quantization demonstrates that these samples act as digital alloyed single quantum wells and not multiple quantum wells. Plots of the magnetoresistance at various gate voltages for the different samples are shown in Fig. 4. At lower (more

negative) gate voltages, a single set of Shubnikov-de Haas oscillations is observed in all of the quantum wells. At higher gate voltages, the second sub-band becomes occupied and an additional set of oscillations is observed for all of the samples. These results demonstrate the formation of a high quality two-dimensional electron gas devoid of parallel conduction in the random alloy quantum well and the digital alloy quantum wells.

From the magnetotransport at various gate voltages, the mobility at different carrier densities can be determined and are shown in Fig. 5 for the different quantum wells. The random alloy digital alloy quantum well has a peak mobility of  $460\,000 \text{ cm}^2/\text{Vs}$  at a  $n_{2\text{DEG}}$  of  $3.13 \times 10^{11} \text{ cm}^{-2}$ , the InAs/GaAs DA quantum well has a peak mobility of  $281\,000 \text{ cm}^2/\text{Vs}$  at a  $n_{2\text{DEG}}$  of  $2.59 \times 10^{11} \text{ cm}^{-2}$ , and the InAs/InGaAs DA quantum well has a peak mobility of  $545\,000 \text{ cm}^2/\text{Vs}$  at a  $n_{2\text{DEG}}$  of  $3.37 \times 10^{11} \text{ cm}^{-2}$ . At least two different devices were fabricated from the same wafer,

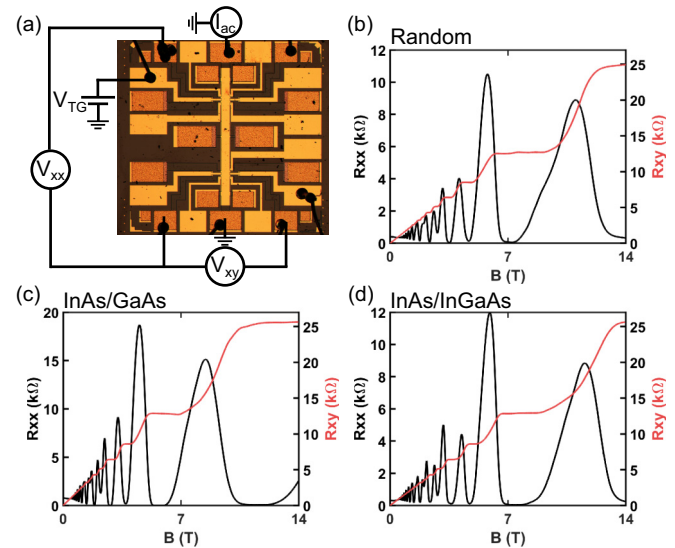


FIG. 3. (a) Optical image of the Hall bar and schematic sample wiring. 2 K magnetotransport of the: (b) random alloy sample at  $n_{2\text{DEG}} = 3.52 \times 10^{11} \text{ cm}^{-2}$ , (c) InAs/GaAs DA sample at  $n_{2\text{DEG}} = 2.78 \times 10^{11} \text{ cm}^{-2}$ , (d) InAs/InGaAs DA sample at  $n_{2\text{DEG}} = 3.60 \times 10^{11} \text{ cm}^{-2}$ .

TABLE I.  $k \cdot p$  results including band gap energy ( $E_g$ ), sub-band spacing ( $E_2 - E_1$ ), first sub-band effective mass ( $m^*$ ), and effective mass nonparabolicity ( $\alpha$ ).

Sample	$E_g$ (meV)	$E_2 - E_1$ (meV)	$m^*$ ( $m_e$ )	$\alpha$
Random Alloy	573	25.7	0.0347	1.955
InAs/GaAs DA	566	24.7	0.0334	2.134
InAs/InGaAs DA	551	23.6	0.0345	2.324

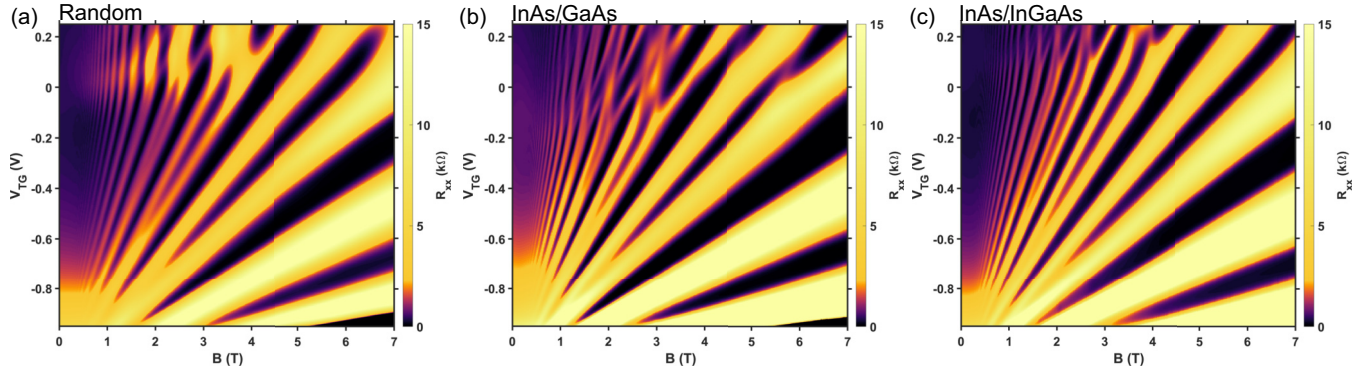


FIG. 4.  $R_{xx}$  at different top-gate voltages and magnetic fields for: (a) random alloy, (b) InAs/GaAs DA, and (c) InAs/InGaAs DA.

revealing an average of 5% variation in the peak mobility. The mobility of the random alloy quantum well is slightly higher than the mobility of  $430\,000\text{ cm}^2/\text{Vs}$  reported in the current state-of-the-art high-In content InGaAs quantum wells [7]. The InAs/InGaAs DA quantum well has a higher peak mobility at a higher carrier density than the random alloy quantum well, while the InAs/GaAs DA samples has a lower peak mobility at a lower carrier density than the random alloy quantum well. From the results shown in Fig. 4, the decrease in mobility after the peak mobility in all of the samples is likely due to inter-sub-band scattering. The electron effective mass is extracted from the thermal damping on the Shubnikov-de Haas oscillations, and these effective masses were used to estimate the Fermi energy at the peak mobility and to estimate the sub-band splitting. These results are summarized in Table II. All of the samples have smaller effective masses than the predicted effective masses from the  $k \cdot p$  calculations, and in the case of the random alloy and the InAs/GaAs DA quantum wells, they have smaller effective masses than  $0.0314 m_e$ , which is the expected bulk effective mass of InGaAs accounting for strain effects calculated using  $k \cdot p$  [24]. This reduction in effective mass is likely due to electron-electron correlations, and has been observed

before in GaAs quantum wells [27]. The sub-band energies estimated from the effective mass and the peak carrier density for the random and the InAs/InGaAs DA are within  $\sim 1\text{ meV}$  of the predicted sub-band energies, and the higher carrier density at the peak mobility for the InAs/InGaAs quantum well is due to the larger effective mass of the InAs/InGaAs sample. However, the InAs/GaAs DA quantum well sub-band energy is significantly different than the predicted, and may be due to the aforementioned potential inaccuracies of the  $k \cdot p$  method for monolayer heterostructures.

The transport ( $\tau_t$ ) and quantum ( $\tau_q$ ) lifetimes of the samples at the peak mobility can be determined with the effective mass, and are given in Table III. The transport lifetimes were calculated from the following equation:  $\tau_t = \mu m^*/e$ . The difference in transport lifetime between the different samples reflects the differences in the mobility, with the InAs/InGaAs DA QW having the highest lifetime and the InAs/GaAs DA QW having the lowest lifetime. The magnetic field onset ( $B_{on}$ ) of the Shubnikov-de Haas oscillations is often correlated with the quantum lifetime and is provided in the table, see the Supplemental Material [28] for the low field Shubnikov-de Haas oscillations. All of the samples have similar  $B_{on}$ , which indicates that the quantum lifetimes are similar. The quantum lifetime was extracted from decay of the amplitude of the Shubnikov-de Haas oscillations [29,30]. From the extracted quantum lifetimes of the samples, the random alloy sample has the lowest quantum lifetime, and the two DA samples have higher lifetimes, with the InAs/InGaAs DA having the highest quantum lifetime. The ratio of the transport lifetimes to the quantum lifetime is also provided in the table. The transport lifetime is significantly higher than the quantum lifetime, consistent with the transport lifetime being insensitive to small angle scattering, while the quantum lifetime is sensitive to all scattering events, and is generally more sensitive to long-range scattering [31]. These results indicate that digital alloying can improve the quantum lifetime in quantum wells.

### C. Scattering mechanisms

To understand the differences in the mobility and the scattering mechanisms for the different samples, the mobilities were modeled using a calculation for the elastic scattering time of electrons in the two-dimensional electron gas [32]. The calculations accounted for background impurity

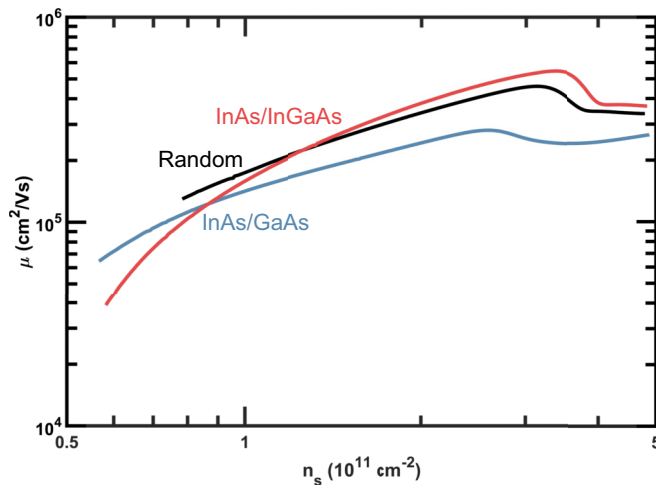


FIG. 5. The dependence of mobility on sheet carrier density for the three different samples. Carrier density was varied by modifying the top gate voltage.

TABLE II. Sample parameters including the peak mobility, carrier density at the peak mobility, the effective mass from thermal damping, the estimated Fermi energy at the peak mobility, and the carrier density at  $V_{TG} = 0$  V.

Sample	$\mu_{\max}$ ( $10^3$ cm <sup>2</sup> /Vs)	$n_{2\text{DEG}}$ at $\mu_{\max}$ ( $10^{11}$ cm <sup>-2</sup> )	$m^*$ ( $m_e$ )	$\varepsilon_f$ at $\mu_{\max}$ (meV)	$n_{2\text{DEG}}$ at $V_{TG} = 0$ V ( $10^{11}$ cm <sup>-2</sup> )
Random Alloy	460	3.13	$0.030 \pm 0.001$	25.0	3.81
InAs/GaAs DA	281	2.59	$0.030 \pm 0.001$	20.7	3.73
InAs/InGaAs DA	545	3.37	$0.033 \pm 0.002$	24.5	3.89

scattering [33], interfacial roughness scattering [34,35], remote impurity scattering [33], and alloy disorder scattering [36]. Zero temperature was assumed and inter-sub-band scattering was not considered. The exact details of the calculations are given in the Appendix. The remote impurity scattering was treated as a fixed sheet charge of  $2 \times 10^{12}$  cm<sup>-2</sup> at the top surface of the quantum well, which is an overestimate of the surface state density of InAlAs [37–40]. However, the exact surface state density of the remote impurities at the surface is found to be not important, as the contribution of remote impurity scattering from the top surface is found to have negligible effect on the mobility of the quantum wells due to the depth of the quantum well from the surface. The remaining parameters used for the mobility modeling were based off previously reported values from modeling InGaAs quantum wells [7]. These parameters were adjusted until good agreement with the experimental data was achieved and are given in Table IV. The transport lifetimes due to the different scattering were calculated independently, and the total mobility was computed using Matthiessen's rule.

The mobilities of the samples at different carrier densities and the calculated mobilities are shown in Fig. 6. The calculated total mobility and the mobility for the different scattering mechanisms are also shown. There is good agreement between the calculated mobility and the measured mobility for all of the samples at higher carrier densities until the peak mobility is reached, where the measured mobility begins to decrease due to inter-sub-band scattering between the first and second sub-bands, which is not accounted for with the mobility calculations. In all of the samples, two distinct regimes can be observed, alloy disorder scattering dominates at higher carrier densities and background impurity scattering dominates at lower carrier densities. This behavior is similar to what has been observed in prior studies of InGaAs quantum wells [7,8]. The measured mobility begins to diverge from the calculated and is lower than what the calculations would predict at carrier densities lower than  $\sim 1 \times 10^{10}$  cm<sup>-2</sup>. This deviation in mobility is likely a metal-insulator transition due to localization of charge carriers. Similar metal-insulator

transitions have been observed before in GaAs [41], AlAs [42], and Si quantum wells [43].

A higher background impurity density is required to accurately model the mobilities of the InAs/GaAs ( $2.4 \times 10^{15}$  cm<sup>-3</sup>) and the InAs/InGaAs ( $1.6 \times 10^{15}$  cm<sup>-3</sup>) digital alloy quantum wells than the random alloy quantum well ( $1.5 \times 10^{15}$  cm<sup>-3</sup>). The background impurity densities extracted from the modeling are similar to what has been previously reported in InGaAs quantum wells [7,8,22]. The InAs/GaAs DA has more interfaces, with the 17 periods of InAs/GaAs, than the InAs/InGaAs DA, with four periods, and has a higher estimated background impurity density than the InAs/InGaAs DA. This trend suggests that the higher background impurity density is due to impurity incorporation at the interfaces of the digital alloy during growth, which has been observed to occur at the interfaces of superlattices grown by MBE [44,45]. The origin of these additional impurities could be from the brief growth interrupt during the growth of the digital alloys. From these results, it is desirable to reduce the number of periods in the superlattice to reduce the background impurity density and therefore the background impurity scattering for the growth of high mobility samples.

The interfacial roughness in the random and InAs/InGaAs digital alloy is estimated from the model to be 6 Å. This value is smaller than the roughness measured by atomic force microscopy of the InAlAs top barrier, which we attribute due to the InGaAs layers being smoother than the InAlAs layers at the growth temperature. The interfacial roughness of the random and InAs/InGaAs DA quantum wells is comparable to prior studies of the interfacial roughness of InGaAs quantum wells [7]. However, the modeled interfacial roughness of the InAs/GaAs is significantly higher, with a roughness of 21 Å. The increased roughness becomes a significant scattering mechanism at higher carrier densities in the InAs/GaAs digital alloy. The increased roughness is likely due to the growth of rougher GaAs islands as the GaAs layer in the InAs/GaAs digital alloy. GaAs has been reported to grow as islands on InAs layers [46]. These results demonstrate that the optimal growth temperature of the constituent layers of the

 TABLE III. The transport lifetimes ( $\tau_t$ ) and quantum lifetimes ( $\tau_q$ ) of the samples at the peak mobility as well as the ratio of the two lifetimes and the onset of Shubnikov de-Haas oscillations ( $B_{\text{on}}$ ).

Sample	$\tau_t$ (ps)	$\tau_q$ (ps)	$\tau_t/\tau_q$	$B_{\text{on}}$ (T)
Random Alloy	7.85	0.21	37.4	0.23
InAs/GaAs DA	4.79	0.27	17.7	0.23
InAs/InGaAs DA	10.23	0.31	33.0	0.22

 TABLE IV. Mobility modeling parameters including alloy disorder potential ( $dV$ ), background impurity density ( $n_{\text{BI}}$ ), interface roughness ( $\Delta$ ), and correlation length ( $\Lambda$ ).

Sample	$dV$ (eV)	$n_{\text{BI}}$ (cm <sup>-3</sup> )	$\Delta$ (Å)	$\Lambda$ (nm)
Random Alloy	0.44	$1.5 \times 10^{15}$	6	13
InAs/GaAs DA	0.44	$2.4 \times 10^{15}$	21	3
InAs/InGaAs DA	0.38	$1.6 \times 10^{15}$	6	13

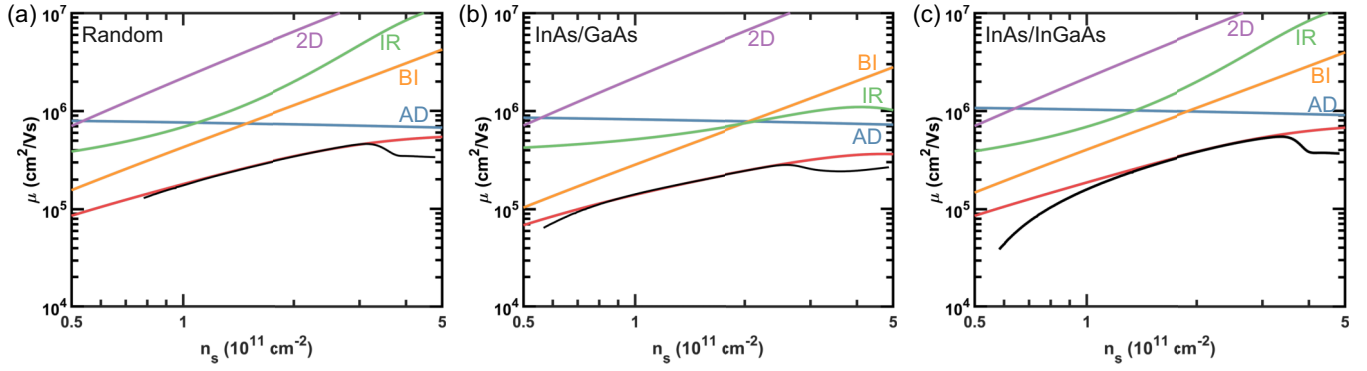


FIG. 6. Experimentally measured mobility and calculated mobility at various sheet carrier densities for the: (a) random alloy, (b) InAs/GaAs DA, and (c) InAs/InGaAs quantum wells. The total mobility and the individual mobilities for the different scattering mechanisms including: interfacial roughness scattering (IR), two-dimensional remote impurity scattering (2D), background impurity scattering (BI), and alloy disorder scattering (AD) are plotted.

digital alloy is an important consideration, and can result in rougher growth and enhanced interfacial roughness scattering.

In order to accurately model the experimental data, the alloy disorder potential in the random alloy quantum well is estimated to be 0.44 eV. This value is larger than the 0.3 eV reported previously in InGaAs quantum wells [7], but closer to the expected value of 0.5 eV of InGaAs [47]. We find that the same alloy disorder potential of 0.44 eV is required to obtain a good agreement to the experimental InAs/GaAs DA mobility curves, which we propose is due to significant intermixing in the InAs/GaAs layers creating alloy disorder. In the InAs/InGaAs digital alloy, the alloy disorder potential is estimated to be 0.38 eV from the modeling, this alloy disorder potential is smaller than the alloy disorder of the random alloy. The reduction in the alloy disorder potential is likely due to the electrons preferentially residing in the InAs regions of the digital alloy, as seen in the  $k \cdot p$  results in Fig. 2(c), and as a consequence the electron do not spend as much time in the regions of the quantum well that possess alloy disorder. The overall increase in mobility observed in the InAs/InGaAs DA quantum well over the random alloy quantum well is due to this reduction in alloy disorder scattering. These results as a whole suggest that digital alloying can be used to reduce alloy disorder scattering in quantum wells and the importance of the heterostructure design and the interfaces in the mobility of digital alloy quantum wells.

#### IV. CONCLUSIONS

In summary, we have demonstrated in high electron mobility InGaAs quantum wells, digital alloys can be used as an alternative to random alloys in semiconductor quantum wells and increase the quantum well mobility by reducing the alloy disorder scattering. Single sub-band transport, the interger quantum Hall effect, and the absence of parallel conduction are observed in the random and digital alloys. However, increased background impurity density is observed in the digital alloys, likely due to incorporation of impurities at the interfaces. The results indicate the digital alloy should be grown with as few periods as possible to improve the mobility of the digital alloy quantum wells over that of the random alloy. Additionally, the quality of the interfaces and

the growth conditions are important, otherwise alloy disorder and enhanced interfacial roughness scattering can be introduced into the digital alloy quantum wells and subsequently reduce the mobility. We believe that our results should be generally applicable to other semiconductor alloys, and can be used to increase the mobility in other material systems.

#### ACKNOWLEDGMENTS

This growth of the quantum wells was supported by University of California Multiple Campus Award No. 00023195. Modeling efforts of the quantum wells was supported by the Department of Energy under Award No. DE-SC0019274. We acknowledge the use of shared facilities of the NSF Materials Research Science and Engineering Center (MRSEC) at the University of California Santa Barbara (Grant No. DMR 2308708) and the Nanotech UCSB Nanofabrication Facility.

#### APPENDIX: MOBILITY MODELING

The InGaAs quantum well with InAlAs barriers envelope wave function  $[\phi(z)]$  over the InGaAs thickness  $L$  is approximated by:

$$\phi(z) = \left(\frac{2}{L}\right)^{1/2} \sin\left(\frac{\pi z}{L}\right)$$

for  $0 \leq z \leq L$  and 0 for all other  $z$ . Only the lowest occupied sub-band is treated. The mobility is defined as:  $\mu = e\tau/m^*$ , where  $e$  is the elementary charge,  $\tau$  is the scattering time, and  $m^*$  is the effective mass.

From the treatment by Stern and Howard [32] using the Born approximation, the scattering time for a scattering mechanism ( $i$ ) at a given Fermi wave vector ( $k_f$ ) is defined as:

$$\frac{\hbar}{\tau_i} = \frac{1}{2\pi\epsilon_f} \int_0^{2k_f} dq \frac{q^2}{\sqrt{4k_f^2 - q^2}} \frac{\langle |U_i(q)|^2 \rangle}{\epsilon(q)^2},$$

where  $q$  is the scattering vector,  $\epsilon_f$  is the Fermi energy computed using a nonparabolic effective mass,  $\hbar$  is the reduced Planck constant,  $\langle |U_i(q)|^2 \rangle$  is the averaged scattering potential associated with the particular scattering mechanism, and  $\epsilon(q)$  is the dielectric function from the random phase

approximation. The dielectric function is defined as:

$$\epsilon(q) = 1 + \frac{q_{\text{TF}}}{q} [1 - G(q)] F_C(q),$$

where  $q_{\text{TF}}$  is the Thomas-Fermi screening wave number  $q_{\text{TF}} = m^* e^2 / 4\pi \epsilon_L \hbar^2$  with the dielectric constant  $\epsilon_L$ ,  $G(q)$  is the generalized form of the local field correction [48], and  $F_C(q)$  is the form factor of the Coulomb interaction of the finite width of the quantum well, defined as:

$$F_C(q) = \int_{-\infty}^{+\infty} dz |\phi(z)|^2 \int_{-\infty}^{+\infty} dz' |\phi(z')|^2 \exp(-q|z - z'|).$$

The scattering potential for interface roughness is [34] of the form:

$$\langle |U_{\text{IR}}(q)|^2 \rangle = \pi F_{\text{IR}}^2 \Delta^2 \Lambda^2 \exp[-(q\Lambda)^2/4],$$

where  $\Delta$  is the interfacial roughness,  $\Lambda$  is the correlation length, and  $F_{\text{IR}}$  is a function that is modified following the treatment by Ref. [35] to include the shift of the ground state by a electric field  $E$ :

$$F_{\text{IR}} = - \left( \frac{\hbar^2 \pi^2}{m^* L^3} + 96 \left( \frac{2}{3\pi} \right)^6 \frac{e^2 m^* L^3 E^2}{\hbar^2} \right).$$

Alloy disorder within the  $\text{In}_{1-x}\text{Ga}_x\text{As}$  quantum well with an alloy disorder potential of  $dV$  leads to a scattering potential [36] of:

$$\langle |U_{\text{AD}}(q)|^2 \rangle = x(1-x) dV^2 \frac{\sqrt{3\pi} a^3}{16} \frac{3L}{2}.$$

Two-dimensional remote ionized impurities with an charged impurity density of  $n_j$  lead to a scattering potential of the form [33]:

$$\langle |U_{2\text{D}}(q)|^2 \rangle = \left( \frac{2\pi e^2}{\epsilon_L} \frac{1}{q} \right)^2 n_j F_{2\text{D}}(q, z_j)^2.$$

$F_{2\text{D}}(q, z_j)$  is the form factor accounting for the distance between the charged impurity layer and the quantum well:

$$F_{2\text{D}}(q, z_j) = \int_{-\infty}^{+\infty} dz |\phi(z)|^2 \exp(-q|z - z_j|).$$

The scattering potential of homogeneously distributed charged background impurities [33] is:

$$\langle |U_{\text{BI}}(q)|^2 \rangle = \left( \frac{2\pi e^2}{\epsilon_L} \frac{1}{q} \right)^2 N_B L F_{\text{BI}}(q),$$

where  $N_B$  is the background impurity density and  $F_{\text{BI}}(q)$  is the form factor for background impurities, defined as:

$$F_{\text{BI}}(q) = \frac{1}{L} \int_{-\infty}^{+\infty} dz_j F_{2\text{D}}(q, z_j)^2.$$

The total scattering time was determined from the individual scattering times and applying Matthiessen's rule:

$$1/\tau = 1/\tau_{\text{IR}} + 1/\tau_{\text{AD}} + 1/\tau_{2\text{D}} + 1/\tau_{\text{BI}}.$$

- 
- [1] H. Kosaka, A. A. Kiselev, F. A. Baron, K. W. Kim, and E. Yablonovitch, Electron  $g$  factor engineering in III-V semiconductors for quantum communications, *Electron. Lett.* **37**, 464 (2001).
- [2] J.-M. Jancu, R. Scholz, E. A. de Andrada e Silva, and G. C. La Rocca, Atomistic spin-orbit coupling and  $k \cdot p$  parameters in III-V semiconductors, *Phys. Rev. B* **72**, 193201 (2005).
- [3] S. N. Holmes, P. J. Simmonds, H. E. Beere, F. Sfigakis, I. Farrer, D. A. Ritchie, and M. Pepper, Bychkov-Rashba dominated band structure in an  $\text{In}_{0.75}\text{Ga}_{0.25}\text{As} - \text{In}_{0.75}\text{Al}_{0.25}$  device with spin-split carrier densities of  $<10^{11} \text{ cm}^{-2}$ , *J. Phys.: Condens. Matter* **20**, 472207 (2008).
- [4] Y. Oreg, G. Refael, and F. von Oppen, Helical liquids and Majorana bound states in quantum wires, *Phys. Rev. Lett.* **105**, 177002 (2010).
- [5] R. M. Lutchyn, J. D. Sau, and S. Das Sarma, Majorana fermions and a topological phase transition in semiconductor-superconductor heterostructures, *Phys. Rev. Lett.* **105**, 077001 (2010).
- [6] S. Datta and B. Das, Electronic analog of the electro-optic modulator, *Appl. Phys. Lett.* **56**, 665 (1990).
- [7] C. Chen, I. Farrer, S. N. Holmes, F. Sfigakis, M. P. Fletcher, H. E. Beere, and D. A. Ritchie, Growth variations and scattering mechanisms in metamorphic  $\text{In}_{0.75}\text{Ga}_{0.25}\text{As}/\text{In}_{0.75}\text{Al}_{0.25}\text{As}$  quantum wells grown by molecular beam epitaxy, *J. Cryst. Growth* **425**, 70 (2015).
- [8] F. Capotondi, G. Biasiol, D. Ercolani, and L. Sorba, Scattering mechanisms in undoped  $\text{In}_{0.75}\text{Ga}_{0.25}\text{As}/\text{In}_{0.75}\text{Al}_{0.25}\text{As}$  two-dimensional electron gases, *J. Cryst. Growth* **278**, 538 (2005).
- [9] M. Kawabe, M. Kondo, N. Matsuura, and K. Yamamoto, Photoluminescence of  $\text{Al}_x\text{Ga}_{1-x}/\text{Al}_y\text{Ga}_{1-y}$  multiquantum wells grown by pulsed molecular beam epitaxy, *Jpn. J. Appl. Phys.* **22**, L64 (1983).
- [10] D. S. Jiang, K. Kelting, T. Isu, H. J. Queisser, and K. Ploog, Luminescence properties of  $(\text{GaAs})_l(\text{AlAs})_m$  superlattices with  $(l, m)$  ranging from 1 to 73, *J. Appl. Phys.* **63**, 845 (1988).
- [11] J. D. Song, D. C. Heo, I. K. Han, J. M. Kim, Y. T. Lee, and S.-H. Park, Parametric study on optical properties of digital-alloy  $\text{In}(\text{Ga}_{1-z}\text{Al}_z)\text{As}/\text{InP}$  grown by molecular-beam epitaxy, *Appl. Phys. Lett.* **84**, 873 (2004).
- [12] S. Z. Ahmed, Y. Tan, J. Zheng, J. C. Campbell, and A. W. Ghosh, Biaxial strain modulated valence-band engineering in III-V digital alloys, *Phys. Rev. B* **106**, 035301 (2022).
- [13] A. K. Rockwell, M. Ren, M. Woodson, A. H. Jones, S. D. March, Y. Tan, Y. Yuan, Y. Sun, R. Hool, S. J. Maddox, M. L. Lee, A. W. Ghosh, J. C. Campbell, and S. R. Bank, Toward deterministic construction of low noise avalanche photodetector materials, *Appl. Phys. Lett.* **113**, 102106 (2018).
- [14] M. G. Peters, B. J. Thibeault, D. B. Young, J. W. Scott, F. H. Peters, A. C. Gossard, and L. A. Coldren, Band-gap engineered digital alloy interfaces for lower resistance vertical-cavity surface-emitting lasers, *Appl. Phys. Lett.* **63**, 3411 (1993).

- [15] J. Jaroszyński, T. Andrearczyk, G. Karczewski, J. Wróbel, T. Wojtowicz, E. Papis, E. Kamińska, A. Piotrowska, D. Popović, and T. Dietl, Ising quantum Hall ferromagnet in magnetically doped quantum wells, *Phys. Rev. Lett.* **89**, 266802 (2002).
- [16] M. Sundaram, S. A. Chalmers, P. F. Hopkins, and A. C. Gossard, New quantum structures, *Science* **254**, 1326 (1991).
- [17] H. L. Störmer, J. P. Eisenstein, A. C. Gossard, W. Wiegmann, and K. Baldwin, Quantization of the Hall effect in an anisotropic three-dimensional electronic system, *Phys. Rev. Lett.* **56**, 85 (1986).
- [18] J. H. Baskey, A. J. Rimberg, S. Yang, R. M. Westervelt, P. F. Hopkins, and A. C. Gossard, Remotely-doped superlattices in wide parabolic GaAs/Al<sub>x</sub>Ga<sub>1-x</sub>As quantum wells, *Appl. Phys. Lett.* **61**, 1573 (1992).
- [19] T. Hoshino and N. Mori, Electron mobility calculation for two-dimensional electron gas in InN/GaN digital alloy channel high electron mobility transistors, *Jpn. J. Appl. Phys.* **58**, SCCD10 (2019).
- [20] N. Pant, W. Lee, N. Sanders, and E. Kioupakis, Increasing the mobility and power-electronics figure of merit of Al-GaN with atomically thin AlN/GaN digital-alloy superlattices, *Appl. Phys. Lett.* **121**, 032105 (2022).
- [21] I.-H. Tan, G. L. Snider, L. D. Chang, and E. L. Hu, A self-consistent solution of Schrödinger-Poisson equations using a nonuniform mesh, *J. Appl. Phys.* **68**, 4071 (1990).
- [22] F. Capotondi, G. Biasiol, I. Vobornik, L. Sorba, F. Giazotto, A. Cavallini, and B. Fraboni, Two-dimensional electron gas formation in undoped In<sub>0.75</sub>Ga<sub>0.25</sub>As/In<sub>0.75</sub>Al<sub>0.25</sub>As quantum wells, *J. Vac. Sci. Technol. B* **22**, 702 (2004).
- [23] P. J. Simmonds, H. E. Beere, D. A. Ritchie, and S. N. Holmes, Growth-temperature optimization for low-carrier-density In<sub>0.75</sub>Ga<sub>0.25</sub>As-based high electron mobility transistors on InP, *J. Appl. Phys.* **102**, 083518 (2007).
- [24] I. Vurgaftman, M. P. Lumb, and J. R. Meyer, *Bands and Photons in III-V Semiconductor Quantum Structures* (Oxford University Press, Oxford, 2020), pp. 275–293.
- [25] D. M. Wood, A. Zunger, and D. Gershoni, Origins of  $k \cdot p$  errors for [001] GaAs/AlAs heterostructures, *Europhys. Lett.* **33**, 383 (1996).
- [26] M. Cankurtaran, H. Çelik, E. Tiras, A. Bayrakli, and N. Balkan, Quantum and transport mobilities of electrons in GaAs/Ga<sub>1-x</sub>Al<sub>x</sub>As multiple quantum wells, *phys. stat. sol.* **207**, 139 (1998).
- [27] A. T. Hatke, M. A. Zudov, J. D. Watson, M. J. Manfra, L. N. Pfeiffer, and K. W. West, Evidence for effective mass reduction in GaAs/AlGaAs quantum wells, *Phys. Rev. B* **87**, 161307(R) (2013).
- [28] See Supplemental Material at <http://link.aps.org/supplemental/10.1103/PhysRevMaterials.8.064601> for low magnetic field magnetotransport of the quantum wells.
- [29] P. T. Coleridge, R. Stoner, and R. Fletcher, Low-field transport coefficients in GaAs/Ga<sub>1-x</sub>Al<sub>x</sub>As heterostructures, *Phys. Rev. B* **39**, 1120 (1989).
- [30] P. T. Coleridge, Small-angle scattering in two-dimensional electron gases, *Phys. Rev. B* **44**, 3793 (1991).
- [31] S. Das Sarma and F. Stern, Single-particle relaxation time versus scattering time in an impure electron gas, *Phys. Rev. B* **32**, 8442 (1985).
- [32] F. Stern and W. E. Howard, Properties of semiconductor surface inversion layers in the electric quantum limit, *Phys. Rev.* **163**, 816 (1967).
- [33] A. Gold, Electronic transport properties of a two-dimensional electron gas in a silicon quantum-well structure at low temperature, *Phys. Rev. B* **35**, 723 (1987).
- [34] H. Sakaki, T. Noda, K. Hirakawa, M. Tanaka, and T. Matsusue, Interface roughness scattering in GaAs/AlAs quantum wells, *Appl. Phys. Lett.* **51**, 1934 (1987).
- [35] R. K. Jana and D. Jena, Stark-effect scattering in rough quantum wells, *Appl. Phys. Lett.* **99**, 012104 (2011).
- [36] G. Bastard, Energy levels and alloy scattering in InP-In(Ga)As heterojunctions, *Appl. Phys. Lett.* **43**, 591 (1983).
- [37] J. S. Hwang, W. Y. Chou, S. L. Tyan, H. H. Lin, and T. L. Lee, Study of surface Fermi level and surface state distribution in InAlAs surface-intrinsic-n<sup>+</sup> structure by photoreflectance, *Appl. Phys. Lett.* **67**, 2350 (1995).
- [38] W. Y. Chou, G. S. Chang, W. C. Hwang, and J. S. Hwang, Analysis of Fermi level pinning and surface state distribution in InAlAs heterostructures, *J. Appl. Phys.* **83**, 3690 (1998).
- [39] G. S. Chang, W. C. Hwang, Y. C. Wang, Z. P. Yang, and J. S. Hwang, Determination of surface state density for GaAs and InAlAs by room temperature photoreflectance, *J. Appl. Phys.* **86**, 1765 (1999).
- [40] J. S. Hwang, G. S. Chang, W. C. Hwang, and W. J. Chen, Photoreflectance studies of surface state density of InAlAs, *J. Appl. Phys.* **89**, 1771 (2001).
- [41] A. Gold, Metal-insulator transition in Al<sub>x</sub>Ga<sub>1-x</sub>As/GaAs heterostructures with large spacer width, *Phys. Rev. B* **44**, 8818 (1991).
- [42] A. Gold, Mobility of thin AlAs quantum wells: Theory compared to experiment, *Appl. Phys. Lett.* **92**, 082111 (2008).
- [43] A. Gold, Mobility and metal-insulator transition of the two-dimensional electron gas in SiGe/Si/SiGe quantum wells, *J. Appl. Phys.* **108**, 063710 (2010).
- [44] T. Achtnich, G. Burri, M. A. Py, and M. Ilegems, Secondary ion mass spectrometry study of oxygen accumulation at GaAs/AlGaAs interfaces grown by molecular beam epitaxy, *Appl. Phys. Lett.* **50**, 1730 (1987).
- [45] S. F. Yoon, H. M. Li, K. Radhakrishnan, and D. H. Zhang, The effect of growth interruption on the photoluminescence linewidth of GaAs/InGaAs quantum wells grown by molecular beam epitaxy, *J. Cryst. Growth* **131**, 1 (1993).
- [46] F. D. Schowengerdt, F. J. Grunthaler, and J. K. Liu, AES and EELFS studies of initial stages of growth of GaAs/InAs/GaAs heterostructures, *MRS Online Proc. Libr.* **144**, 201 (1988).
- [47] D. K. Ferry, Alloy scattering in ternary III-V compounds, *Phys. Rev. B* **17**, 912 (1978).
- [48] A. Gold and L. Calmels, Correlation in Fermi liquids: Analytical results for the local-field correction in two and three dimensions, *Phys. Rev. B* **48**, 11622 (1993).